AGU ADVANCING EARTH AND SPACE SCIENCE

Earth and Space Science

RESEARCH ARTICLE
10.1029/2022EA002586

CubeSat GPS Observation of Traveling Ionospheric Disturbances After the 2022 Hunga-Tonga Hunga-Ha'apai Volcanic Eruption and Its Potential Use for Tsunami Warning

Shin-Chan Han[1], Simon McClusky[2], T. Dylan Mikesell[3], Lucie Rolland[4], Emile Okal[5], and Craig Benson[6]

[1]School of Engineering, University of Newcastle, Callaghan, NSW, Australia, [2]Geoscience Australia, Symonston, ACT, Australia, [3]Norwegian Geotechnical Institute, Oslo, Norway, [4]Université Côte d'Azur, Géoazur, Valbonne, France, [5]Department of Earth and Planetary Sciences, Northwestern University, Evanston, IL, USA, [6]Skykraft Pty Ltd., Braddon, ACT, Australia

Key Points:

- A constellation of CubeSats detected traveling ionospheric disturbances (TIDs) caused by the Hunga-Tonga Hunga-Ha'apai volcanic eruption
- The slant total electron content anomaly at high altitudes was as large as 10 TECU and remained significant at the antipode 16 hr after the eruption suggesting the propagation speed of ~350 m/s
- TIDs observed a few hours before the conventional tsunami reach the Australian coasts leave time for tsunami source assessment

Correspondence to:
S.-C. Han,
shin-chan.han@newcastle.edu.au

Citation:
Han, S.-C., McClusky, S., Mikesell, T. D., Rolland, L., Okal, E., & Benson, C. (2023). CubeSat GPS observation of traveling ionospheric disturbances after the 2022 Hunga-Tonga Hunga-Ha'apai volcanic eruption and its potential use for tsunami warning. *Earth and Space Science*, *10*, e2022EA002586. https://doi.org/10.1029/2022EA002586

Received 20 AUG 2022
Accepted 12 MAR 2023

Author Contributions:

Conceptualization: Shin-Chan Han, Simon McClusky, T. Dylan Mikesell
Formal analysis: Shin-Chan Han
Investigation: Shin-Chan Han, Lucie Rolland
Methodology: Shin-Chan Han, Simon McClusky, T. Dylan Mikesell
Resources: Shin-Chan Han
Software: Shin-Chan Han, Simon McClusky
Validation: Shin-Chan Han, T. Dylan Mikesell, Lucie Rolland
Visualization: Shin-Chan Han

Abstract Multiple passages of the atmospheric (Lamb) waves were recorded globally after the Hunga Tonga-Hunga Ha'apai (HTHH) volcanic eruption on 15 January 2022. The waves perturbed the ionosphere and produced traveling ionospheric disturbances (TIDs) that were observed from the ground network of Global Positioning System (GPS) receivers. This study presents new observations of TIDs at higher altitudes (>550 km) from CubeSat GPS tracking data. The satellite sampling along many CubeSat orbits enable to map broader spatio-temporal patterns of the TID propagation compared to ground receivers. Due to the larger spatial coverage over a shorter period of time, the CubeSat measurements provide complementary information to stationary ground receivers. We found that the amplitude of the HTHH-induced ionospheric perturbations at high altitudes (>550 km) are as large as 10 TECU (1 TECU = 10^{16} electrons/m^2) in slant total electron content between CubeSats and GPS satellites. The TIDs traveled along with the Lamb waves and were recorded by CubeSats above India 12 hr after the eruption and at the antipode of the eruption 16 hr after. These suggest that the ionospheric disturbances reached to the high altitudes and traveled globally as a speed of ~350 m/s. The TIDs were also detected by CubeSats above the Australian continent several hours before the (conventional) tsunami made landfall on the Australian coasts. We discuss a new opportunity to study the upper ionosphere and its coupling with the solid Earth and to develop advanced monitoring systems of geohazards by the advent of low-cost small satellite technology.

Plain Language Summary CubeSat of a shoe box size is a low-cost technology that can be used as a platform of various science payloads. The outputs become increasingly reliable and relevant not only to the science community, but also to the public. Global Positioning System receivers are being widely used to locate CubeSats and experiment on the atmosphere via the radio wave refraction. This study reports CubeSat GPS observations of the atmospheric perturbations after the Hunga Tonga-Hunga Ha'apai (HTHH) volcanic eruption on 15 January 2022. Triggered by the HTHH explosion, the atmospheric waves propagated throughout the entire globe and vertically to the ionosphere populated with electrons. The CubeSat GPS receivers detected significant disturbances in the upper ionosphere (>550 km altitudes) traveling with the atmospheric waves, reaching even to the antipode of the volcano 16 hr after the eruption. It was also noticed that such ionospheric disturbances were detected above the continents before the tsunami waves make landfall. The study suggests new opportunity to explore how the upper atmosphere responds to extreme events occurred on the solid Earth and demonstrates how the atmospheric sensing based on affordable small satellite constellation can be used to monitor extreme events such as volcanic eruptions, tsunamis, and earthquakes.

1. Introduction

The Hunga Tonga-Hunga Ha'apai (HTHH) underwater volcanic eruption (20.5°S, 175.4°W) that occurred on 15 January 2022 generated what are known as co-volcanic ionospheric disturbances (CVIDs). Many CVIDs were observed locally (e.g., Astafyeva et al., 2022; Matoza et al., 2022) and a few CVIDs were observed globally (e.g., Aa et al., 2022; Hong et al., 2022; Themens et al., 2022; Zhang et al., 2022). These CVIDs were generated by eruption-driven acoustic (>3 mHz) and gravity (<3 mHz) waves that propagated from Earth's surface through the atmosphere up to ionospheric heights (e.g., Astafyeva, 2019; Meng et al., 2019). Co-volcanic ionospheric

Writing – original draft: Shin-Chan Han, Simon McClusky, T. Dylan Mikesell, Lucie Rolland, Emile Okal, Craig Benson

disturbances manifest as variations in electron density of the ionosphere, which are measured as variations of total electron content (TEC). The CVID are often quasi-periodic with periods of 4–30 min (e.g., Dautermann et al., 2009; Shults et al., 2016) and can be observed by many different methods which are sensitive to TEC, for example, Global Navigation Satellite System (GNSS) or one of its kind, Global Positioning System (GPS).

Co-volcanic ionospheric disturbances fall into a class of phenomena known as traveling ionospheric disturbances (TIDs). As these are moving disturbances, they are characterized by not only their wave-like periodicity, but also by their velocity, that is, their speed and propagation direction (e.g., Heki & Ping, 2006). Different acoustic and gravity waves in the atmosphere travel with different velocities, and therefore, one can often associate specific TIDs with specific types of atmospheric phenomena, for example, the Lamb wave of the HTHH eruption. This association is important from a natural hazard perspective because TID observations can be used to infer information about the source processes that generated the atmospheric waves (e.g., Afraimovich et al., 2013; Calais et al., 1998; Dautermann et al., 2009; Heki, 2019; Jin et al., 2016; Komjathy et al., 2012; Rakoto et al., 2018; Rolland et al., 2013), and the community is working toward monitoring these phenomena in (near) real time (e.g., Brissaud & Astafyeva, 2022; Komjathy et al., 2016; Martire et al., 2023).

Ionospheric disturbances generated by atmospheric phenomena are well understood to first order (e.g., Kherani et al., 2012). The ionosphere is a dynamic place, with charged particles constantly moving around. Charged particles in the ionosphere move due to electric fields, collisions with other particles (e.g., neutral molecules or atomic O), ion diffusion, and thermal effects (i.e., nighttime vs. daytime). In most TEC studies related to natural hazards, one considers a model whereby velocity disturbances in the neutral atmosphere molecules couple their momentum into the ionized particles of the ionosphere plasma through collisions. This leads to changes in the electron density along a satellite-receiver line-of-sight, which provide the observations of TEC disturbance. The disturbance in the neutral atmosphere is caused by the natural hazard and the observed TEC disturbance is an observable manifestation of this neutral atmosphere perturbation.

Themens et al. (2022) demonstrated the global ionospheric disturbances after the HTHH eruption using global ground networks of GNSS stations, and Zhang et al. (2022) subsequently reported the disturbances propagated worldwide at primary speeds of 300–350 m/s and lasted for nearly four days. Zhang et al. (2022) also concluded the Lamb wave energy leak into the thermosphere producing the TID reaching at high altitudes. In this study, we probe the upper limits of Earth's atmosphere and the associated perturbations caused by the HTHH eruption and the induced tsunami. We use a constellation of CubeSats equipped with GNSS receivers, orbiting at ∼560 km altitudes with a wide range of inclinations, rather than more commonly used ground-based GNSS receivers. In this regard, we are using the (slant) TEC measurements between CubeSats and GPS satellites to study perturbations well above (>500 km) most previous studies of natural hazard-induced TEC perturbations integrated in the entire ionosphere. The physics of the processes at play in the higher altitudes are less understood, and this type of CubeSat observation will lead to improved understanding of less-explored high-altitude processes. This will also enhance the analysis of ground-based measurements by separating the effects from the higher altitudes.

In addition, the faster orbital motion of CubeSats enables sampling of wider regions of the ionosphere over short time spans (e.g., ∼9,000 km is covered in ∼20 min) and, when operated in a constellation ("network") of numerous small satellites, they enable us to map out the detailed spatio-temporal patterns of the TIDs; something that is much more difficult to achieve with ground-based GNSS receivers particularly over the ocean. The coverage of CubeSat data is certainly global and not only limited to land and near coast regions as are the ground-based GNSS networks. With CubeSats we can observe vast expanses over the open oceans and it means that the spatial sensitivity to TID detection increases significantly using CubeSat data to provide complementary information to the traditional ground-based observation methods. Here we present a new set of HTHH-induced TID observations from CubeSat GPS data, investigate the TIDs related to the Lamb wave propagation (e.g., Kanamori et al., 1994), and we discuss new opportunities to improve early warning of tsunamis that may result from a variety of geohazards.

2. Quality of CubeSat GPS Tracking Data

The TEC between a CubeSat and a GPS satellite can be computed by various linear combinations of GPS tracking data (pseudorange and carrier phase); for example, between (a) coarse acquisition (C/A) code and L1 carrier phase, (b) precision code (P2) and L2 carrier phase, (c) L1 and L2 carrier phases, and other similar combinations for different frequency measurements. As inter-channel biases, initial phases, and phase ambiguities are unknown, these combinations all infer only biased TEC along the radio ray path (i.e., the line-of-sight) between a GPS

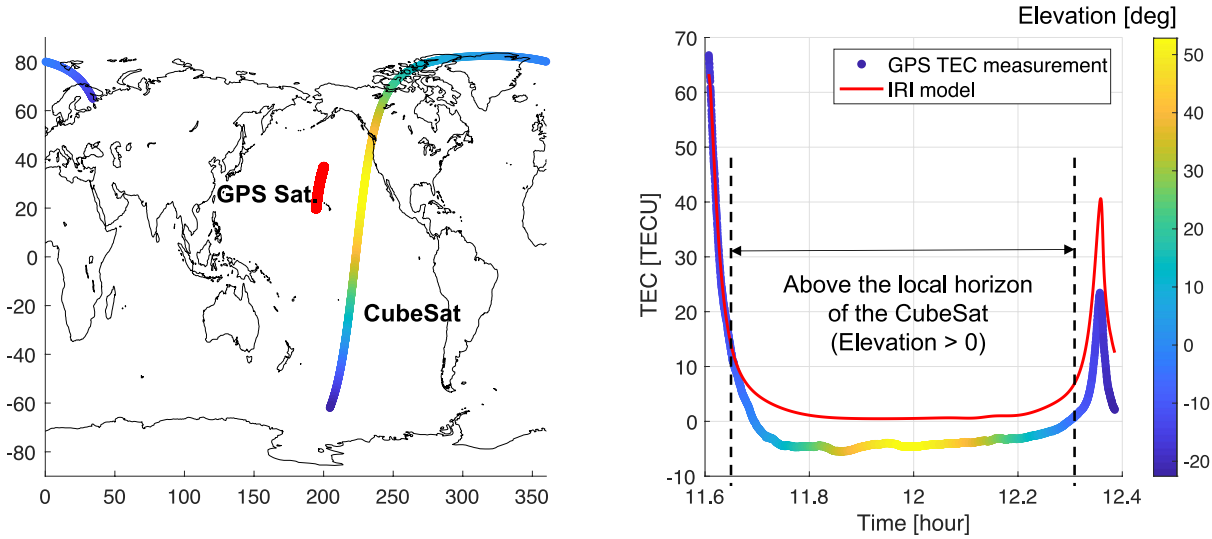

Figure 1. (left) An example of ground tracks of a CubeSat FM107 and Global Positioning System (GPS) satellite G07 for ~45 min (right) The total electron content time series between the CubeSat and the GPS satellite computed from the L1 and L2 carrier phase data and from the International Reference Ionosphere model. An arbitrary value (5 TECU) was added to the GPS data for plotting clarity. The color indicates the elevation of the GPS satellite seen from the CubeSat. Note that the measurements below the local horizon are affected by larger electrons at altitudes below the CubeSat (<560 km).

satellite and a CubeSat, also known as slant TEC. Due to large ranging noise in the code data, the most precise observation of relative TEC is derived from the L1 and L2 carrier phase combination (such as combination c). This combination is available from dual-frequency GNSS receivers that we will discuss mostly in this study; however, there is also growing interest in TEC change derived from the single-frequency instruments (e.g., the technology in most smart phones, combination (a) that we will also cover in this section.

Han et al. (2021, 2023) processed the dual (L1-L2) frequency GPS data available from Spire Global's CubeSats with small patch antennas and oscillators for precision orbit determination (POD) and demonstrated kinematic orbit solutions comparable with the reduced dynamic solutions at a 10 cm level. The POD GPS tracking data are available at 1 Hz and include the GPS satellites tracked even below the local horizon with an elevation angle as low as −22°. Han et al. (2021, 2023) showed that the CubeSat carrier phase data present a few mm of ranging noise while the pseudorange data show a few m of noise. Considering the delay or advance of ranging by 1 TECU (TECU = 10^{16} electrons per m^2) is 16 and 27 cm for L1 and L2 radio waves, respectively, the L1-L2 phase combination is sensitive to TEC change as small as a few percentages of 1 TECU.

Figure 1 (left) shows the ground tracks of a CubeSat at ~560 km altitude and of a GPS satellite at ~20,000 km altitude during a half orbit (~45 min) of the CubeSat. The colors along the CubeSat ground track indicate the elevation angle of the GPS satellite as seen from the CubeSat. The (biased) slant TEC data computed from the L1-L2 phase measurements are presented through time (Figure 1, right); the predicted TEC from the International Reference Ionosphere (IRI-2016) model (Bilitza, 2018) are presented for comparison. An arbitrary value is added to the GPS TEC data for comparison to the IRI model. The TEC increases significantly (a few tens of TECU) as the elevation decreases and goes below zero. This is because GPS radio rays propagate through the high-electron-density ionospheric F-layers (200–300 km altitude) when the elevation is below zero. Due to this strong TEC variability at low elevation angles, the TEC anomalies studied here, associated with the HTHH eruption, will be restricted to the TEC measurements obtained from the GPS satellites during periods of positive elevation angle. Thus, we consider only the perturbations in the upper ionosphere above the CubeSat altitude (>560 km).

The so-called single-frequency TEC measurement computed from the C/A code and L1 phase combination is also examined due to an interest in using single frequency (L1) receivers and antennas. Figure 2 compares the raw (1 Hz) single-frequency TEC data, its smoothed version (low pass filtered below 20 mHz), and the raw L1-L2 phase combination data (i.e., the so-called dual-frequency TEC data). We present data from 14 January 2022 (before the HTHH eruption, left) and from 15 January 2022 (after the HTHH eruption, right) to highlight the size of CVID signals in comparison to other variabilities. We present the same pair of CubeSat (FM129) and GPS satellite (G31) along almost identical ground tracks over the Pacific; the ground tracks of this case are presented

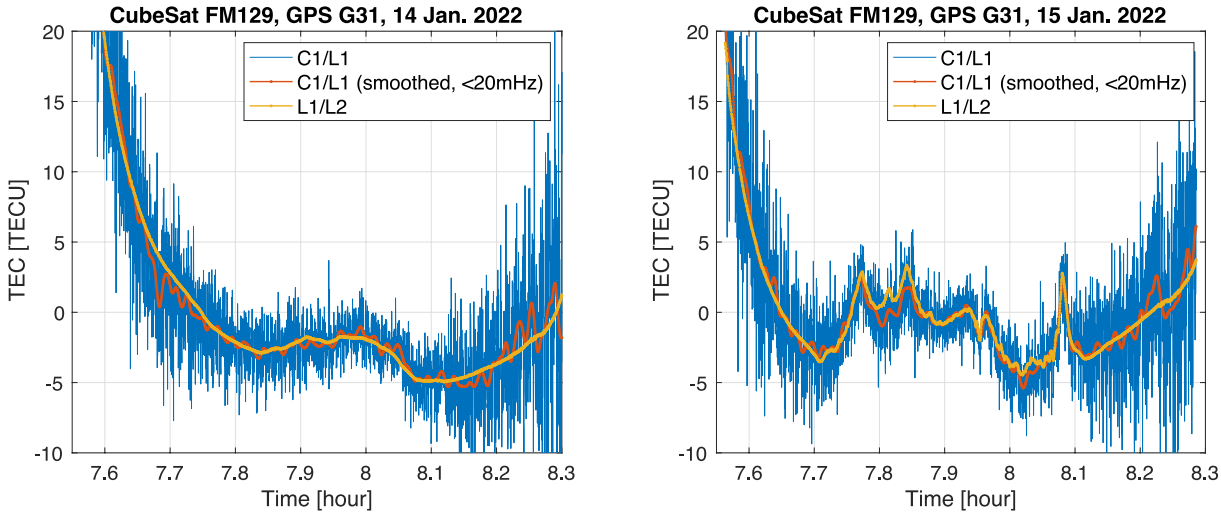

Figure 2. The 1 Hz total electron content measurements from the raw C/A code and L1 carrier phase data (blue), the low-pass filtered (<20 mHz) C/A-L1 time series (red), and the raw L1-L2 carrier phase data (yellow) between CubeSat FM129 and Global Positioning System satellite G31 on 14 (left) and 15 (right) January 2022. The two days cover nearly identical ground tracks of the CubeSat over the Pacific (Figure 3). The several TECU anomalies observed on 15 January are the traveling ionospheric disturbances (TIDs) triggered by the volcanic eruption (see the following text and Figure 3 for detail). Although noisy, but the large TID signals are also detectable in the single frequency measurements.

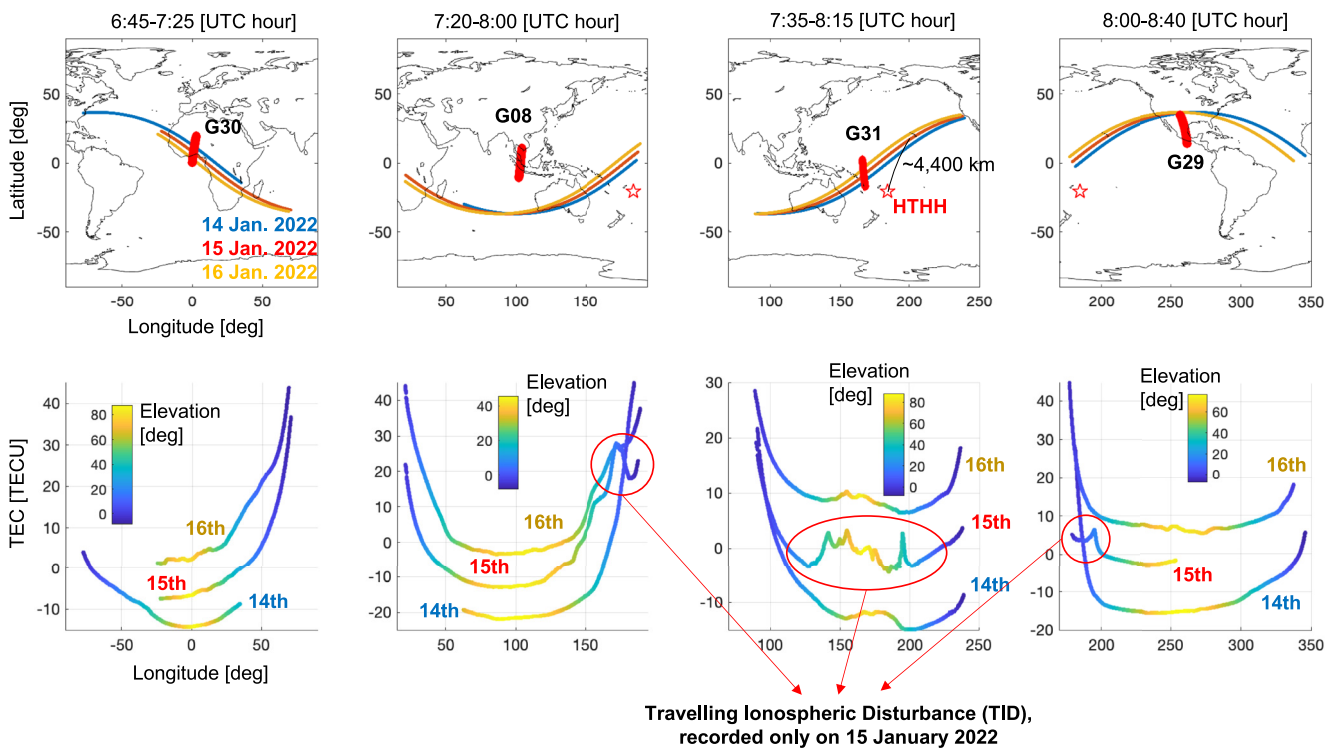

Figure 3. (top) Ground tracks of the CubeSat and Global Positioning System (GPS) satellites before (14 January), on (15 January), and after (16 January) the Hunga Tonga-Hunga Ha'apai (HTHH) volcanic eruption. The CubeSat FM129 orbited from west to east. Four different GPS satellites (G30, G08, G31, and G29) were examined at different longitudes of 0°, 100°, 170°, and 260°E, respectively, at different times. (bottom) The total electron content measurements from each GPS satellite for the 3 days. The color indicates the elevation of the GPS satellite seen from the CubeSat. Traveling ionospheric disturbances were detected only on 15 January and only around the Pacific; this includes the high-elevation data from G31, as well as the low-elevation data from G08 and G29 when the CubeSat was within ~4,400 km of the HTHH volcano around ~3.5 hr after the eruption.

in Figure 3. Given that the ionospheric anomaly after the HTHH eruption is so large (several TECUs), although noisier, the single frequency measurements (C/A code & L1 phase combination) also show similar perturbations to the high-quality dual-frequency measurements. For smaller events, the dual-frequency TEC data will be able to detect smaller anomalies, around a few percentages of 1 TECU, which is more than 100 times smaller than the detection threshold with single-frequency measurements.

3. TEC Changes Due To the HTHH Volcanic Eruption

We processed the dual-frequency (L1-L2 carrier phase) tracking data collected via the zenith-pointing POD antenna every second from one of the Spire Global's CubeSats, Flight Module 129. The FM129 is orbiting at an altitude of ~560 km with a low inclination of ~37°; we show that the low-inclination orbit is particularly useful to monitor the time-evolution of the atmospheric perturbation in the Pacific after the HTHH volcanic explosion. The TEC data between FM129 and different GPS satellites are computed from the L1 and L2 carrier phase data. We first looked at the ground tracks and the elevation angles of GPS satellites, as well as the measured TEC on 14, 15, and 16 January 2022. We analyze these three days and different GPS satellites to identify the signature of TIDs triggered by the HTHH volcanic eruption, which started at approximately 04:30 (UTC) on 15 January 2022.

For the rest of this study, we analyze the slant TEC measurements without converting them to the zenith direction, because the rapid change of transmitter (GPS) and receiver (CubeSat) geometry does not tolerate accurate computation of vertical TEC from slant TEC by a simple projection. Considering the speed of orbiting receivers, the CubeSat TEC data must be interpreted as spatial samples rather than time series at a particular location, unlike the ground-borne data.

The continuous tracking data from each pair of the CubeSat and GPS satellites are typically available without a loss of lock for 30–40 min (one third to one half of a CubeSat orbit). We select four GPS satellites (G30, G08, G31, and G29) as examples. Figure 3 presents each of the four cases, altogether covering 06:45–08:40 UTC. Each column displays a different GPS satellite for 40 min over each of the 3 days. For this period, the GPS satellites (red ground tracks) are relatively stationary compared to the CubeSat (colored ground tracks). Moreover, the GPS are centered over the equatorial region with average longitudes of 0°, 100°, 170°, and 260°E, respectively. The ground tracks of the GPS satellites are almost identical for the three different days, while those of the CubeSat shift slightly (thin blue, red, and yellow curves, respectively, for the three different days, top panels).

In the bottom panels of Figure 3, we compare the TEC measurements between the CubeSat and the GPS satellite along the longitude of the CubeSat ground track shown in the upper panels. The elevation angle of each GPS satellite seen from the local horizon of the CubeSat is indicated in different color. The TEC measurements on three different days are presented with arbitrary values (±10 TECU) introduced for clarity. As introduced previously, the increasing TEC with decreasing elevation angle is the primary characteristic observed in the data over all days. In addition to this elevation-angle dependence, the TEC measurements from satellite G31 (third column) show fluctuations as large as 10 TECU on 15 January 2022 between longitude 130°–200°E (data within annotated oval); note again that this is the slant TEC value between the CubeSat and the GPS satellite. These fluctuations are significantly larger and of shorter wavelength than background variations observed in all other TEC measurements presented in the bottom panel. These TEC fluctuations are also observed by G08 at the easternmost part (data within annotated circle, second column) and by G29 at the westernmost part (data within annotated circle, fourth column). See also the G30 data showing no significant TEC fluctuation at the opposite hemisphere (first column); some weak traces found on 16th might be remanent signals of the HTHH.

The TEC fluctuations are observed at radial distances up to ~4,400 km from the HTHH volcano approximately 3.5 hr after the largest eruptive phase. Given these fluctuations occur only on 15 January, we interpret these as TEC anomalies associated with the HTHH eruption. The earliest arriving anomaly appears to propagate at a speed ~350 m/s (4,400 km divided by 3.5 hr), which is faster than conventional tsunami wave propagation in the open ocean and close to the speed of the atmospheric Lamb wave propagation (Amores et al., 2022; Matoza et al., 2022; Zhang et al., 2022). Therefore, we infer that these TEC observations are likely TIDs related to the Lamb wave from the eruption, which is perturbing the atmosphere at heights above 560 km, the altitude of the CubeSat.

4. High-Altitude TIDs and the HTHH Lamb Wave

The Lamb wave is a type of acoustic-gravity wave that propagates in the atmosphere along the surface of the Earth with a mean speed of ~317 m/s. It was originally described by Lamb (1911), and the more general

theory of the modes supported by various models of atmosphere was given by Press and Harkrider (1962) and Harkrider (1964). In particular, they showed that their detailed properties are subtle functions of the precise thermodynamic structure of the atmospheric column, controlled by high-altitude weather patterns, and thus expected to vary both laterally and temporally, for example, seasonally. Note however that these authors limited their investigations to the first 220 km of the atmospheric column.

Prior to the HTHH explosion, an event comparable in nature but probably larger occurred on 27 August 1883 at Krakatoa, with ocean-coupled air waves observed on maregraphs as far away as Colón (Panama, then Colombia) (Harkrider & Press, 1967). Smaller, but generally similar waves were also observed on seismometers following the Tunguska meteorite explosion on 30 June 1908 (Ben-Menahem, 1975). In addition, Lamb waves were systematically observed and quantified following the larger atmospheric nuclear tests, culminating with "Tsar' Bomba" on 30 October 1961 (Harkrider, 1964; Wexler & Hass, 1962).

Multiple passages of the HTHH Lamb wave were recorded by barometric stations worldwide, including throughout the Australian and American continents, with amplitudes of a few hPa after the eruption (Amores et al., 2022; Matoza et al., 2022). To further understand the observed high-altitude TEC anomalies, we compare a Lamb wave propagation model to the CubeSat GPS TEC measurements. The global atmospheric pressure perturbations due to Lamb wave propagation are taken from the 2D numerical simulation by Amores et al. (2022). In this model the air temperature governs the phase velocity of the Lamb wave. In this simulation the temperature is vertically averaged from 2 m above sea level to the top of troposphere, and the temperature varies through time and space as the Lamb wave propagates around the globe.

Figure 4 presents a series of (slant) TEC measurements between CubeSat FM129 and various GPS satellites (G23, G30, and G31) on 15 January 2022; each row shows a different time range. The CubeSat and GPS ground tracks are presented in the left column. The time (UTC hour) of the measurements is indicated with different colors along the CubeSat tracks, and the predicted Lamb wave pressure perturbation is indicated by cyan. The Lamb wave propagation starts at the HTHH volcano (a red star). The inner and outer bounds of the circular cyan zone indicate the Lamb wave arrival at Earth's surface at the start and end time of the CubeSat measurements, respectively. The three GPS satellites all together cover a total of ∼10 hr after the HTHH eruption. The middle column shows the CubeSat TEC time series with the same color used in the CubeSat ground tracks. This provides a visualization to understand the TEC fluctuations in a spatio-temporal context. The right column presents the same TEC time series over the longitude of the CubeSat ground track. In all cases, the CubeSat orbited from southwest to northeast.

As before, the high TEC with low elevation angle is a notable feature in all time series. The first row of Figure 4 shows the observations immediately after the major eruption at 04:30 UTC. There is no anomaly observed with G23 at this time. After one CubeSat orbit (∼90 min) a noticeable (slant) TEC anomaly is observed with G23 in the vicinity of the volcano, with fluctuations as large as 8 TECU (Figure 4, second row). A TID is clearly observed. Moreover, the timing of the TID onset and demise (magenta dashed lines) are consistent with those of the CubeSat entering and leaving the domain of the atmospheric perturbation due to the Lamb wave (second row, left column). The width of the observed TID anomaly is a rough measure of the spatial extent of the perturbed atmosphere after the eruption (second row, right column). For the case of G23, the TID is observed from 06:08 to 06:29 in UTC hour and from 150° to 210°E in longitude.

For comparison with the ground measurements, the GNSS station at the Samoan island recorded the very large vertical TEC decrease as much as 10–20 TECU around 05:00 UTC (See Figure 1 of Aa et al., 2022 and Figure 1 of Astafyeva et al., 2022), which may be a manifestation of giant shock waves traveled as fast as ∼700 m/s and prevailed only over the near field (Astafyeva et al., 2022; Zhang et al., 2022). Also note that the original (slant) TEC measurements would be even larger by a factor of 1.5, considering the elevation of the GNSS satellites the studies used.

We next consider the G31 measurements over nearly the same UTC time range (Figure 4, third row). The size and duration of the TID anomaly is similar to the G23 observation, which is expected given the overlapping time range between the two. However, the long wavelength (background) change is different due to the different geometry and elevation angle between the CubeSat and the GPS satellites. After another CubeSat orbit (∼90 min), FM129 passes the HTHH region again between 7.6 and 8.3 UTC hours (Figure 4, fourth row). The observed TID anomaly expands in space as the Lamb wave propagates. The fourth passage of the CubeSat (Figure 4, fifth row)

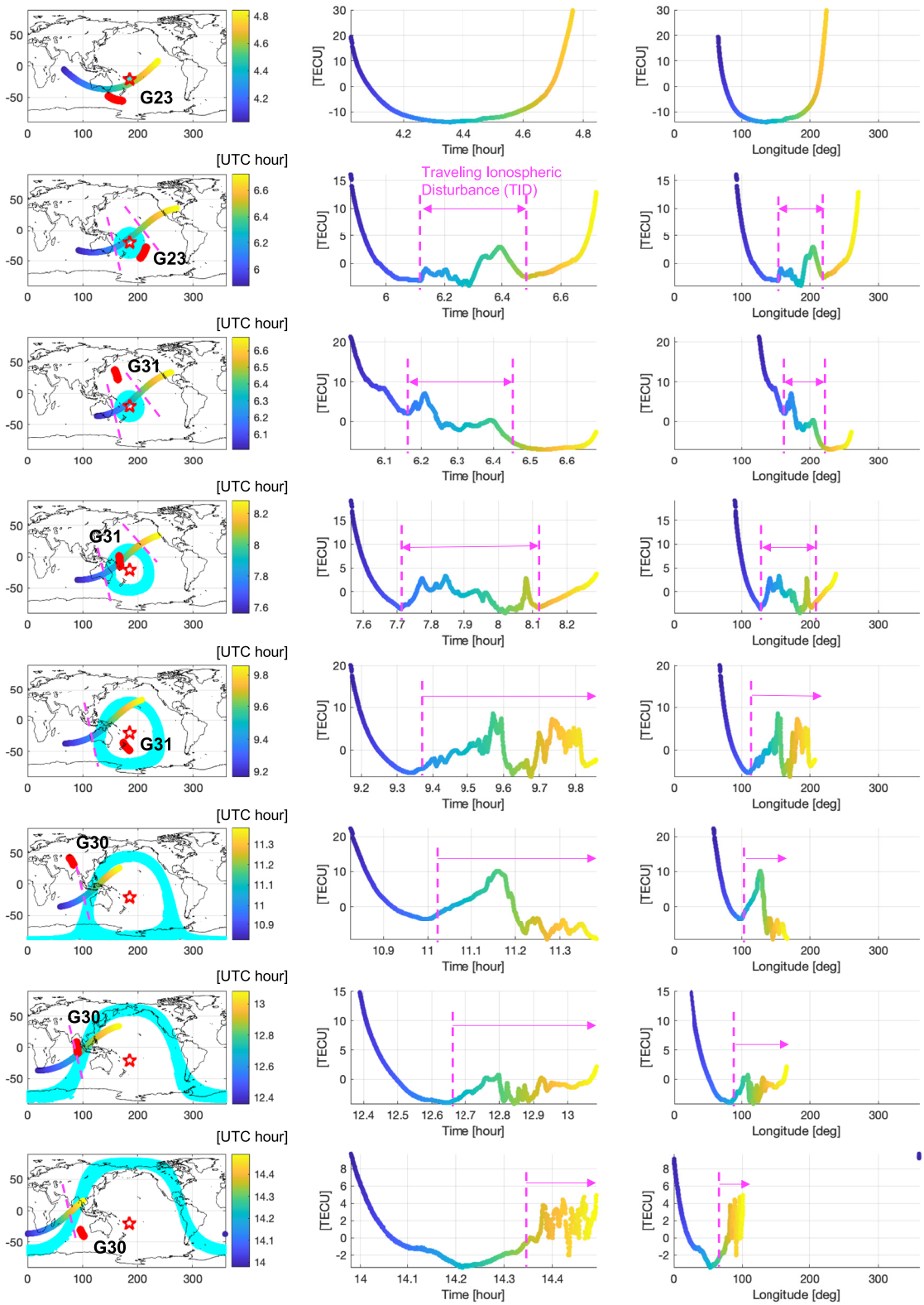

Figure 4.

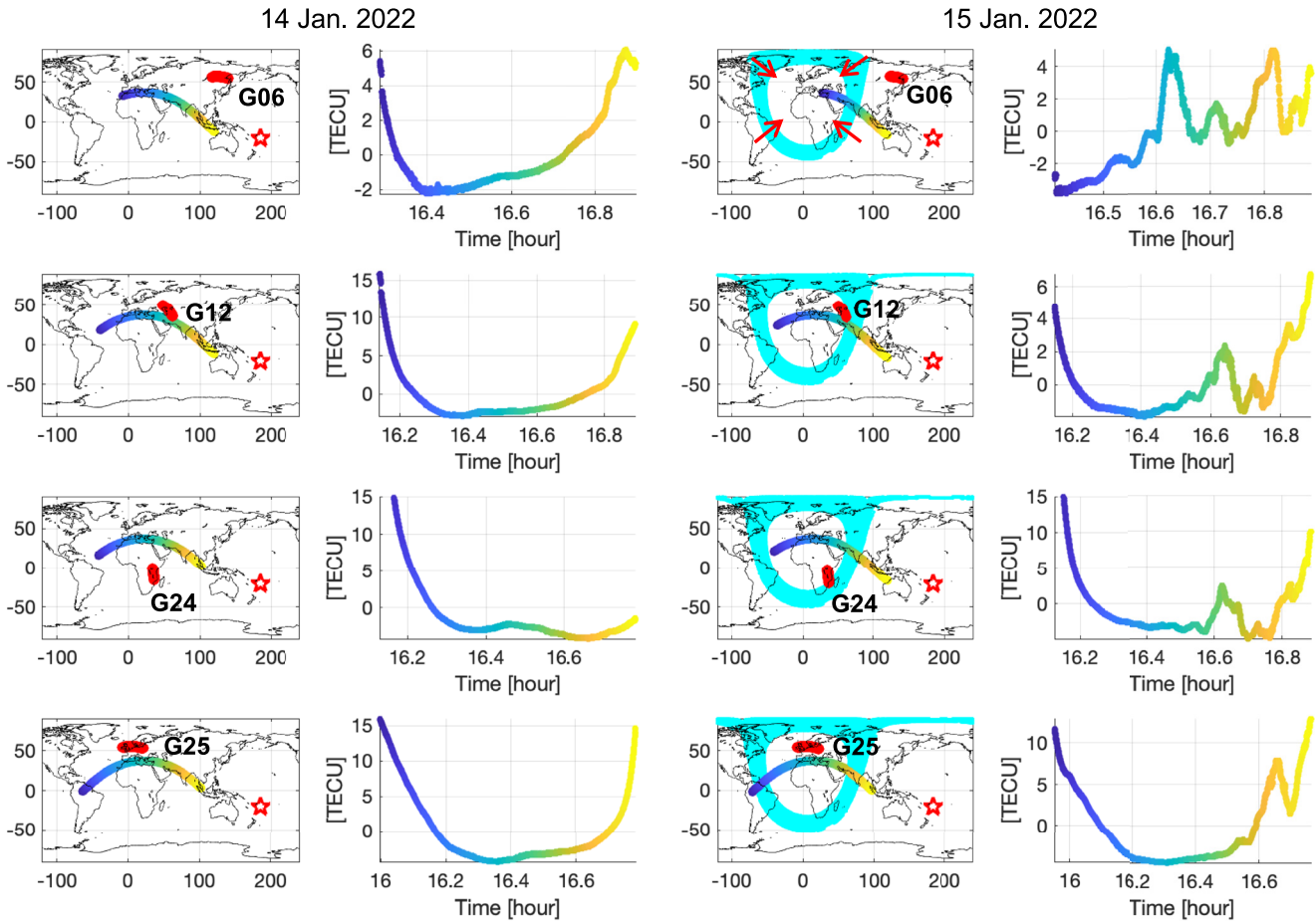

Figure 5. Examples of CubeSat observations of traveling ionospheric disturbances (TIDs) at remote location above India approximately 12 hr after the Hunga Tonga-Hunga Ha'apai volcanic eruption. Four Global Positioning System satellites were used with the CubeSat orbiting around India at that time on 14 and 15 January 2022. Note that the atmospheric waves propagated more than halfway around the globe start to converge to the antipode near the southern tip of Algeria (red arrows). The large and sharp total electron content anomalies (likely the TID induced by the volcanic eruption) were detected only when the CubeSat intersected the atmospheric wave (cyan) from west to east and only on 15 January.

also detects the TID anomaly. The CubeSat observation of the onset of TID indicates that the atmospheric disturbance arrived at the west coast of Australia (115°E) between 09:00 and 10:00 UTC (~5 hr after the eruption), then the CubeSat lost the tracking of G31. The last three rows of Figure 4 show observations with GPS satellite G30. Three consecutive CubeSat orbits detect the westward propagation of the atmospheric perturbation. Ten hours after the eruption, at 14:30 UTC, the TID is detected at the Bengal Bay, east of India.

5. Global TID Observations

With continual propagation of the atmospheric perturbation, the TID is detected in remote areas like India. We observe another low-inclination CubeSat, FM117, orbiting across India at 16:00–17:00 UTC and examine the corresponding GPS TEC data. Figure 5 presents the ground tracks of FM117 and GPS satellites G06, G12, G24, and G25, as well as the measured TEC time series for 14 and 15 January 2022. The Lamb wave propagation model is also shown on 15 January. Around this time (~12 hr after the eruption), the first passage of

Figure 4. Spatio-temporal evolution of the traveling ionospheric disturbances (TIDs) detected by a series of Global Positioning System (GPS) satellites with the CubeSat. (left) Ground tracks of the CubeSat and GPS satellites during the time (UTC hour) indicated with color. The predicted arrival of the atmospheric Lamb waves is depicted with cyan color. The dashed magenta lines indicate the CubeSat's entrance into and exit from the Lamb wave atmosphere disturbance. (middle) The measured total electron content (TEC) time series with the same color used in the ground track to facilitate understanding of the data with the ground locations. (right) The same TEC data but presented with the longitude of the ground tracks to help to understand the spatial extension of the TID anomaly over time. Three GPS satellites were used to monitor the propagation of the atmospheric disturbance over 11 hr following the Hunga Tonga-Hunga Ha'apai eruption.

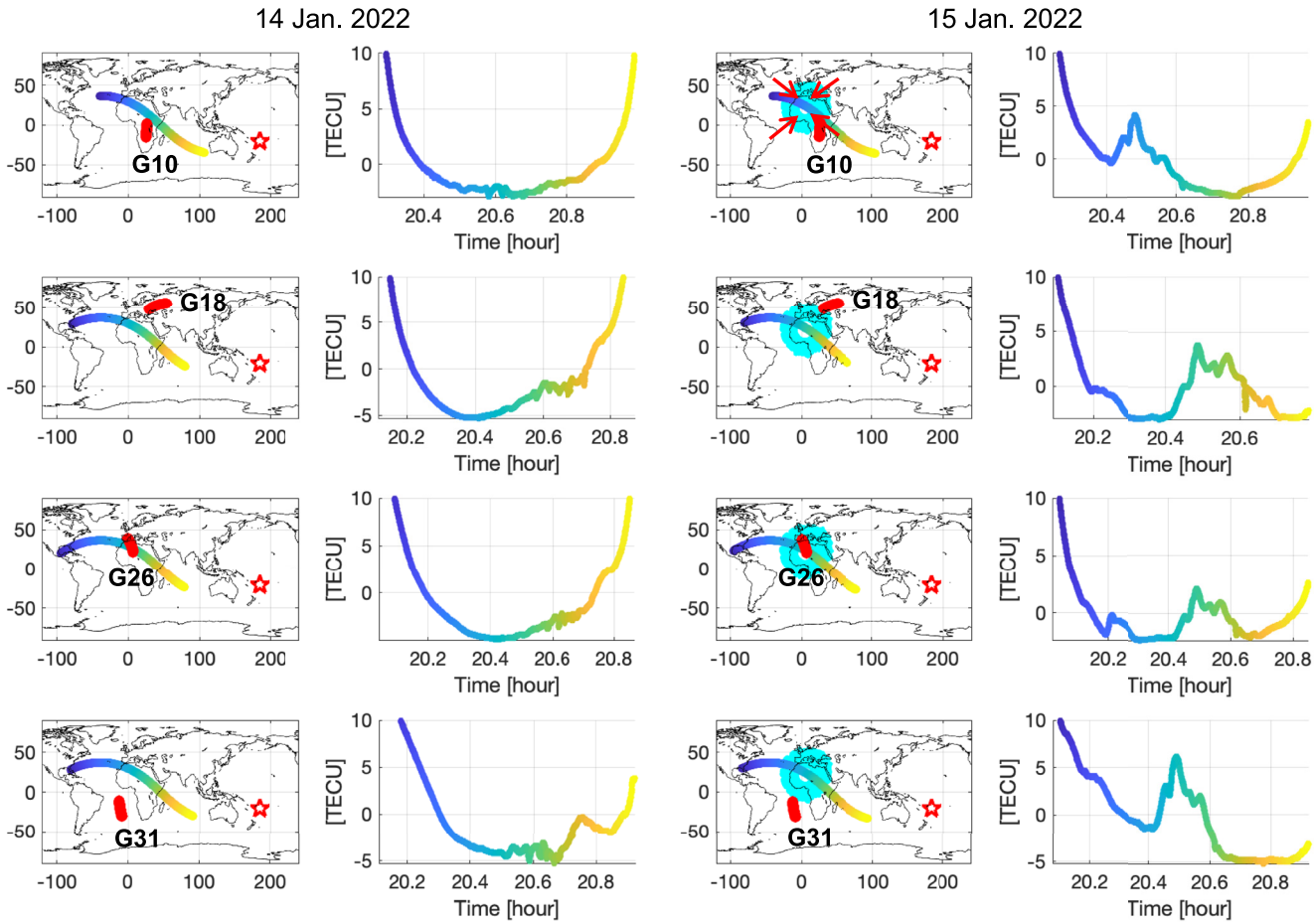

Figure 6. The same as Figure 5, but around the antipode, Algeria, North Africa, 16 hr after the Hunga Tonga-Hunga Ha'apai (HTHH) volcanic eruption. The total electron content anomalies were detected on 15 January and when the CubeSat intersected the Lamb wave front converging to the antipode. Note that the amplitude of the traveling ionospheric disturbance remains significant, even at this location, opposite the globe to the HTHH volcano and 16 hr after the major eruption.

the atmospheric Lamb wave is predicted and the wave begins to converge toward the antipode of the HTHH volcano, located approximately at the extreme Southern tip of Algeria. The direction of the wave propagation is indicated by the red arrows in the top row of Figure 5. FM117 observes the atmospheric wave above India around 16:30 UTC; thus, this high-altitude TID propagates over long distances and can be measured by CubeSats and GPS satellites globally.

The TEC fluctuations occur only after the CubeSat enters the zone of the atmospheric perturbation. Interestingly, the magnitude of the TID is still as large as the TID observed over the Pacific—on the order of several TECU. This is in agreement with barograph observations at ground level which remain on the order of a few hPa during the first four passages of the air wave. It argues for a high quality factor (perhaps 1,000 or more) for the air wave at frequency of <2 mHz. Zhang et al. (2022) and Heki (2022) observed multiple global passages of the HTHH Lamb wave in TEC data recorded in the US continent and Japan, respectively (assuming TEC perturbations at 300 km altitude), indicating that the high-altitude TIDs remain large relative to the natural background TEC fluctuations.

Going further in time, a significant TID is also observed far from the source near the eruption antipode. We examine the data from another low inclination CubeSat, FM115, that orbited over North Africa around 20:30 UTC (16 hr after the eruption). Four GPS satellites G10, G18, G26, and G31 tracked by FM115 are used to study the TEC around the antipode. The TEC time series for approximately the same period and the same orbit but from different GPS satellites is presented for 14 and 15 January 2022 (Figure 6). In this case, the CubeSat FM115 intersected the leading atmospheric Lamb wave from the northwest and exited through the southeast. A significant TID anomaly is only observed on 15 January when the CubeSat meets the front of the atmospheric waves.

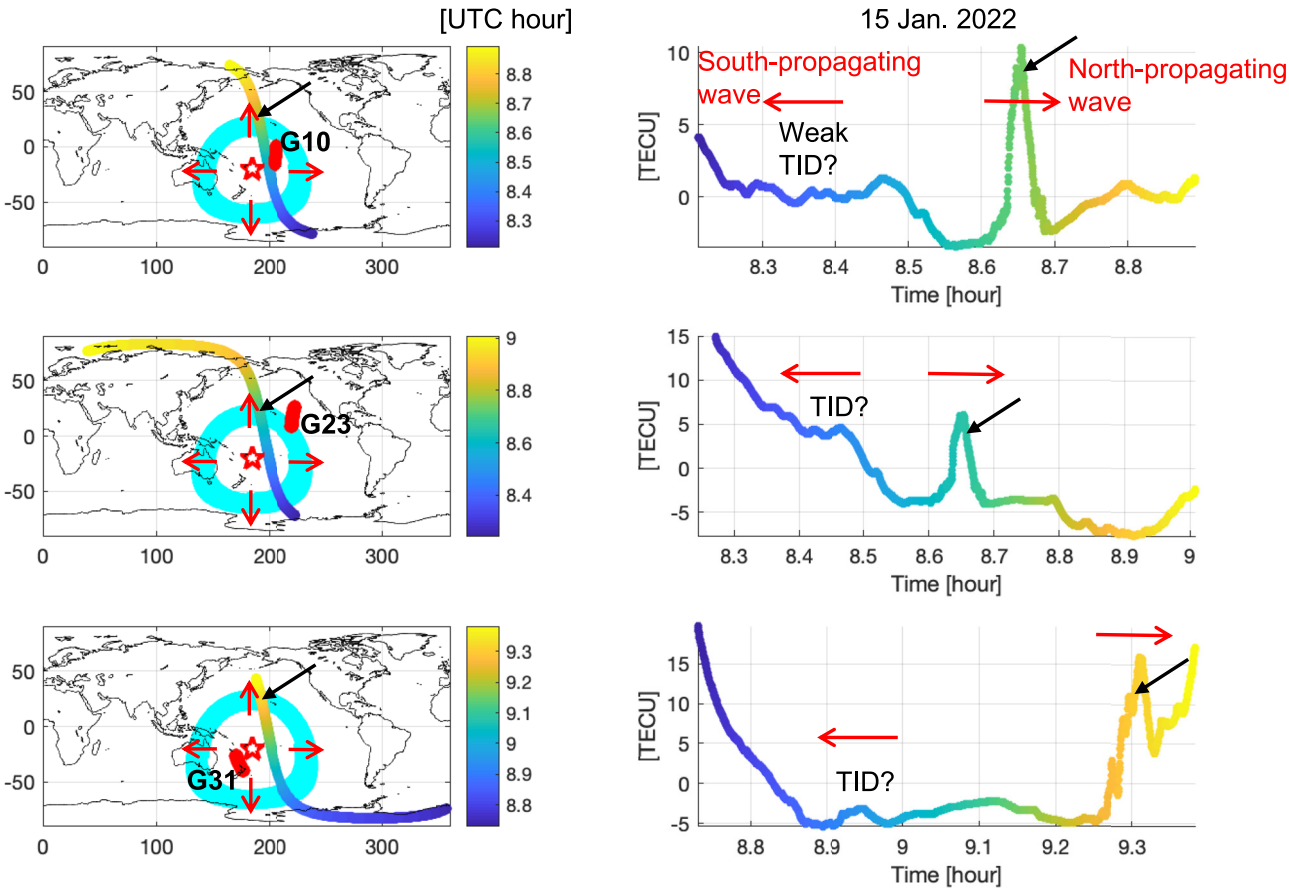

Figure 7. The total electron content (TEC) measurements evidence the more strongly northward propagation of traveling ionospheric disturbances (TIDs) that may be due to the coupling between neutral particles with the plasma and the local geomagnetic field vector. This series of TEC data were obtained from a CubeSat in a polar orbit. The CubeSat orbited from south to north. When the CubeSat intersected the northward propagating wave (the predicted Lamb wave in cyan color), it detected strong TID anomalies, as large as 10 TECU (marked with black arrows), while the measurement across the southern wave is indistinguishable from the background variability. The strong northward perturbation in the ionosphere is expected from ground events that occur in the southern hemisphere due to the plasma motions (anti-)parallel to the direction of the geomagnetic field lines.

Although there are preexisting (slant) TEC anomalies at ~1 TECU on 14 January, possibly associated with the remnant from the geomagnetic storm (Zhang et al., 2022), the TID signal induced by the HTHH eruption is clearly distinguished. The amplitude of TID anomaly is still on the order of a few TECU indicating a persistently strong atmospheric perturbation even at the antipode of the eruption 16 hr later. This measurement of the first arrival of the ionospheric disturbances and its timing are consistent with the Lamb wave propagation.

6. Strong Northward Propagation

The motions of electrons in the ionosphere, unlike the motions of neutral particles, have a directional dependence. Recall that the geomagnetic field controls the motion of the ionosphere particles (e.g., Heelis, 2004). For the near field around the HTHH eruption located in the south hemisphere, we expect to observe stronger TID northward where the neutral particle motions by the acoustic wave tend to be parallel to the local geomagnetic field vector north of the HTHH eruption (Astafyeva, 2019; Rolland et al., 2013). This is an illustration on how such geomagnetic field dip angle northward-southward differences contribute to the observed asymmetry. This north-south different behavior is also typical for gravity waves (Zhao et al., 2020) and can be extrapolated to Lamb waves.

Thus, we analyze CubeSat, FM100, which orbits at a high inclination of 97° (a Sun-synchronous orbit), between 08:00 and 09:00 UTC on 15 January 2022 (Figure 7). FM100 crosses the HTHH region from south to north and the GPS satellites G10, G23, and G31 are used to investigate the north-south difference of TID amplitudes. According to the Lamb wave propagation model, FM100 crosses over the northern and southern fronts

of the atmospheric disturbance, intersecting the southward propagation zone roughly 25 min before entering the northward propagation zone. All TEC observations from three different GPS satellites clearly show a strong perturbation (∼10 TECU, measured as in slant TEC) when the CubeSat crosses over the northward propagating zone (marked with black arrows). The peak TIDs are recorded at the latitudes of 20°–25° N. On the contrary, the TEC anomalies observed over the southward propagating zone are not so distinct from other low-amplitude fluctuations in the TEC.

Moreover, we can assume that the sharp and large (about 10 TECU) TEC increase in Figure 7 is peaking when the CubeSat to GPS satellite line-of-sight is parallel to the TID wavefront, integrating the electron density perturbation constructively on a large distance. This happens when satellites G10 and G23 that respectively sound on the south-eastern and eastern side of the CubeSat have an elevation angle of about 50° (calculated from the GPS and CubeSat orbit geometry). We can thus hypothesize that the observed wavefronts are inclined upward with respect to the local horizontal. This wavefront geometry is consistent with an ionospheric perturbation forced by a large scale gravity wave originating from the HTHH volcano (e.g., Figure 9b of Hickey et al., 2009). The various sounding geometries offered by the GPS satellites could help at better understanding the 3D propagation of the observed TIDs. However, we cannot exclude a contribution of the conjugate effect investigated by Lin et al. (2022) to explain the large TEC increase observed near Hawaii islands, at about 20°N of latitude in Figure 7, which happens to be close to the northern hemisphere conjugate point of the volcanic source.

7. Discussion: Lamb Waves and Tsunamis

The tide gauge at Lord Howe Island (New South Wales, Australia) recorded an initial sea level fluctuation of 0.1 m about 2.5 hr after the eruption (∼07:00 UTC), followed by much larger sea level fluctuations up to 1.0 m when the conventional tsunamis waves arrived about 4.5 hr after the eruption (∼09:00 UTC, traveling at ∼200 m/s). Such sea level fluctuation observations were initially enigmatic, but now are understood as being driven by the atmospheric pressure (Lamb) wave (Kubota et al., 2022). The coupling of atmospheric waves to the oceanic basins resulted in sea level fluctuations observed much earlier than conventionally predicted tsunami waves (Omira et al., 2022), as the atmospheric waves (and thus TID) travel faster than the tsunami waves. This further drives an idea of warning of incoming tsunami by detecting its imprint in the atmosphere well before it arrives on the coasts (e.g., Coïsson et al., 2015).

We analyze the TEC data with the prospect of detecting atmospheric disturbances before tsunami arrivals in mind. The top panels of Figure 8 present the ground tracks of CubeSat FM129 and GPS satellites G27, G31, G10, and G32, as well as the predicted atmospheric (Lamb) wave propagation during 07:30–08:20 UTC (left panel), and the corresponding TEC measurements (right panel). The tsunami wave front is also depicted based on the wave propagation model (NOAA's National Centers for Environmental Information, https://ngdc.noaa.gov/hazard/img/tsunami-timeline/). The TID anomalies in the TEC measurements from all four GPS data align with each other, including their onsets, which occurred over the eastern part of Australia around 7.8 UTC. The northward propagation, could explain the strong peaks we observe near Hawaii around 8.1 UTC. These TID measurements indicate essentially when and where the atmospheric disturbances occurred after the eruption; these findings can be used to estimate the source and predict the incoming waves in ocean and atmosphere, including the tsunami. Additionally, during the period of TID detection over the Australian continent, the front of the (conventional) tsunami wave was still ∼2 hr away from the east coast of Australia.

The second example (bottom panels of Figure 8) comes from the same CubeSat 3 hr later and from different GPS satellites. By then the atmospheric wave had propagated further west and passed Perth, Western Australia. The CubeSat intersected the predicted atmospheric perturbation at 11:00 UTC, when there is a detectable TID onset in the TEC data. At this time, the tsunami wavefront just passed Tasmania and reached Perth 3–4 hr later; note that the atmospheric wave propagates along great circles, while the tsunami must detour around continental masses—another advantage of using the atmosphere for tsunami source assessment and subsequent warning. These two examples demonstrate the atmospheric perturbation detection by CubeSats a few hours before tsunami arrival at the eastern and western coasts of Australia.

Both cases of the CubeSat (slant) TEC measurements (Figure 8 top and bottom panels) were further analyzed in relation with speeds of various waves. First, we applied a high-pass filter (>2 mHz or, equivalently, <∼4,000 km with a speed of CubeSat of ∼8 km/s) to effectively remove the background TEC variation changing mostly with

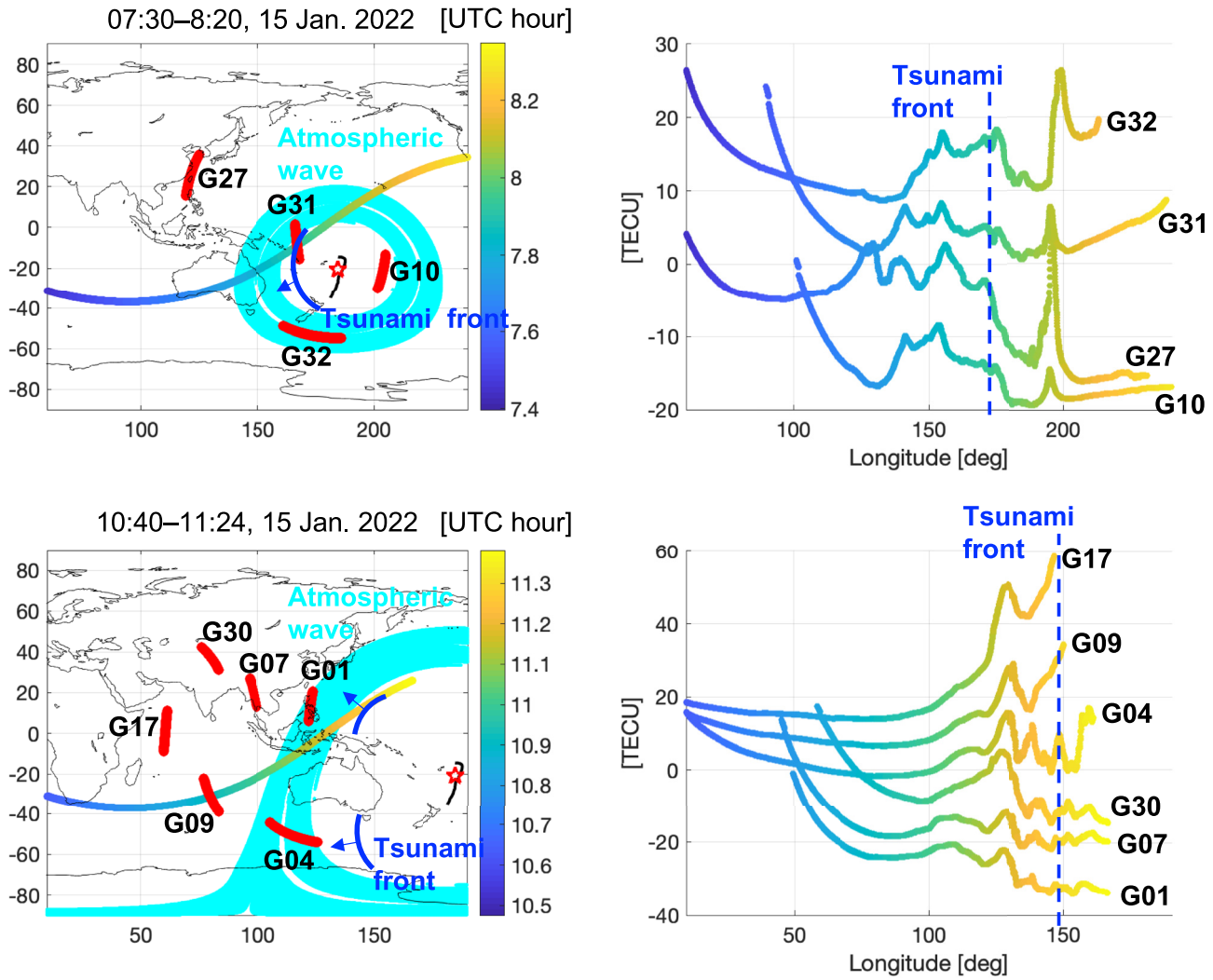

Figure 8. (top-left) The ground tracks of the CubeSat (colors representing the hours of flight), Global Positioning System (GPS) satellites G27, G31, G10, and G32 (red), and the atmospheric wave propagation (cyan) depicted during the period of 07:30–08:20 UTC on 15 January 2022. The CubeSat orbits from southwest to northeast. The Hunga Tonga-Hunga Ha'apai volcano is shown as a red star. The predicted tsunami wavefront is shown in blue with an arrow. (top-right) The time series of total electron content measurements along the longitude of the CubeSat trajectory from different GPS satellites. The traveling ionospheric disturbance (TID) is observed above the eastern part of the Australian continent, while the tsunami wave front is still ~2 hr away from the east coast of Australia. (bottom panels) The same CubeSat data as the top panels but from 10:40–11:24 UTC and from GPS satellites G30, G07, G17, G01, G09, and G04. By then, the atmospheric wave reached and passed the west coast of Australia. The TID is detected on many GPS satellites, while the tsunami wave just passed Tasmania and was ~4 hr away from the west coast. These examples demonstrate that the CubeSats observed multiple TIDs a few hours ahead of the expected tsunami arrival at the eastern and western coasts of Australia.

altitudes. The left panels of Figure 9 present the filtered TEC between different GPS satellites and the CubeSat FM129, similarly to the right panels of Figure 8. The right panels of Figure 9 present the filtered TEC data with the ordinate representing the distance of the CubeSat from the HTHH volcano and the abscissa showing the UTC time. This presentation is useful to identify characteristic speeds of different waves in the filtered TEC measurements. Considering the speed of CubeSats (GNSS receivers), 10–30 times faster than atmospheric and gravity waves, the CubeSat TEC measurements can be seen as spatial samples of TID over a wider region covered by a single GNSS receiver; this is in contrast to temporal sampling of TEC obtained from stationary ground GNSS receivers.

The identified waves in the filtered TEC data exhibit the TID as fast as 500 m/s (G27) over the Australian continent around UTC 7.7 hr. The TIDs with a speed of 300–400 m/s are more commonly identified from G10, G27, G31, and G32 around UTC 7.8 hr including the sharp anomaly traveled with a speed of 350 m/s and detected over Hawaii around UTC 8.1 hr. All these perturbations are consistent with the atmospheric (Lamb) waves. In addition, the TIDs with a speed of 200 m/s were observed around east of Solomon islands at UTC 7.9–8.0 hr.

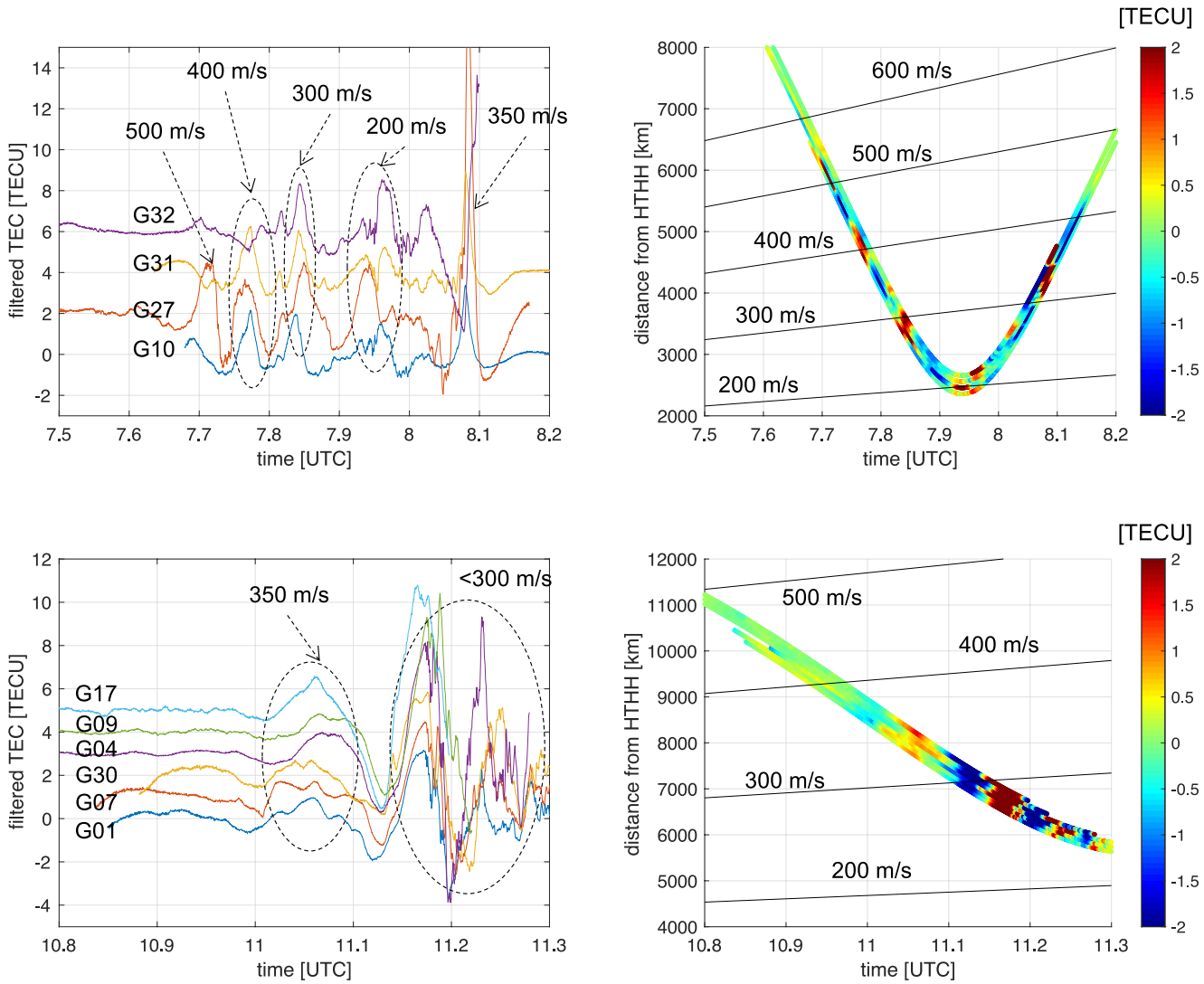

Figure 9. (left) The high-pass filtered CubeSat total electron content measurements similar to the right panels of Figure 8. (right) The filtered data are presented with UTC time (abscissa) and the distance from the Hunga Tonga-Hunga Ha'apai volcano (ordinate) to identify various speeds of wave propagation. The solid black lines present different speeds for the reference. Note that the atmospheric Lamb wave propagates with speeds of 300–400 m/s while the tsunami gravity wave travels with an average speed of ~200 m/s in the open ocean.

Although a thorough numerical modeling of full waveform is needed such as in Coïsson et al. (2015) and Meng et al. (2015), this TID of 200 m/s is consistent with the tsunami and the associated gravity wave propagation. Around 11 hr in UTC (bottom panels of Figure 9), a series of TIDs were identified with a speed of 350 m/s around Indonesia, likely being induced by the Lamb wave. They were followed by the waves propagating with slower speed less than 300 m/s.

With a constellation ("network") of CubeSats, equipped with GNSS receivers, it will be possible to "map" where atmospheric perturbations are heading prior to TID detection by ground-based GNSS receivers that are stationary and waiting for the TIDs to arrives. Such early detection may also be possible only when ground receivers are available around the event locations. Due to the fast orbital speed (~7.8 km/s) of CubeSats, one can investigate large spatial areas over a small amount of time. To further assess the potential of using CubeSat to study hazard related atmospheric perturbations, we processed GPS data from 15 CubeSats, including 5 with low inclination and 10 polar orbits (note, however, that nearly 50% of the GPS data are missing in the polar orbit CubeSats). As can be seen in the example data presented so far, the TID signals manifest themselves as high-frequency perturbations in the measured TEC data and they appear when the CubeSats are at and inside

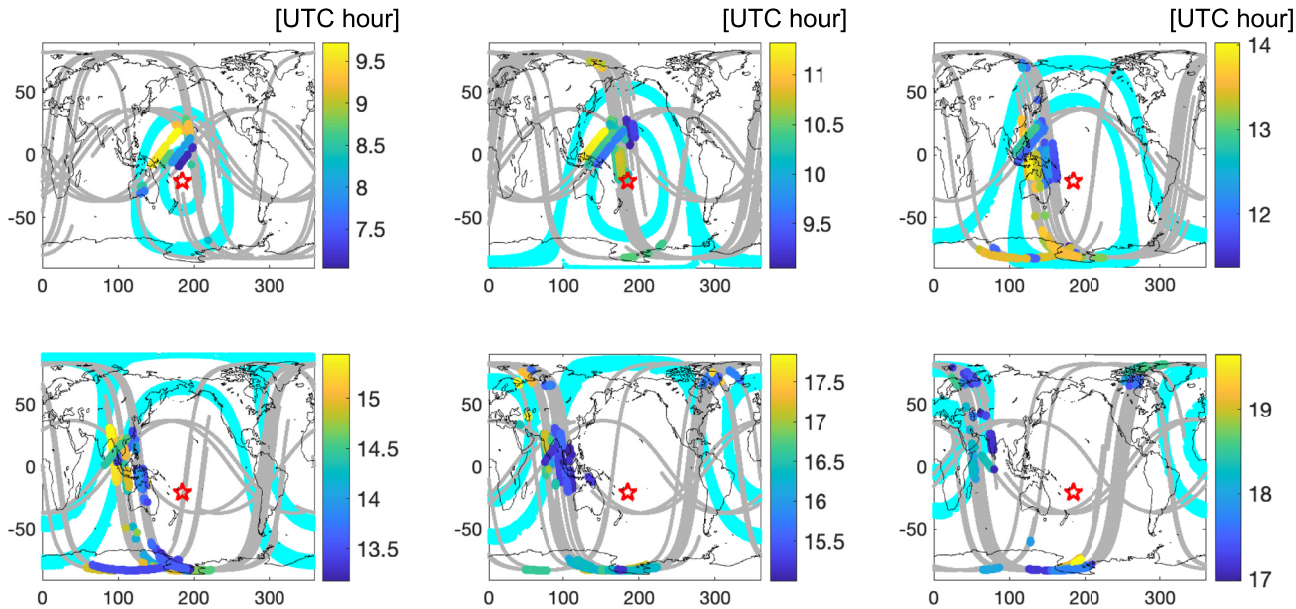

Figure 10. The timing and location of the traveling ionospheric disturbances (TIDs) as detected by a constellation of 15 CubeSats (5 low-inclination + 10 polar) with multiple Global Positioning System satellites. The atmospheric waves propagated widely from 07:00 to 20:00 UTC. The inner and outer circles with cyan color indicate the Lamb wave arrivals at the beginning and the end of the time interval shown in each map. The gray dots indicate the ground tracks of all CubeSats used, and the thick color marks overlying the gray identify hour and location when the high-frequency total electron content (TEC) anomalies were detected from the TEC time series. A simple search for high-frequency TEC anomalies identifies the spatio-temporal TID migration consistent with the atmospheric waves, using the constellation of CubeSats.

of the zone of atmospheric disturbance. We apply a (Morse) wavelet analysis to determine the UTC times when high frequency energy is present in the TEC measurements. Using a simple threshold search of high-frequency (>10 mHz) TEC energy, we determine the timing and location of possible TID signatures.

Figure 10 presents the ground tracks of all CubeSats considered from 07:00 to 20:00 UTC in 2.5-hr bins. The predicted Lamb wave propagation at the beginning (the inner circle) and the end (the outer circle) of the period corresponding to each map is shown as well (~2.5 hr difference each case). The colored marks along the CubeSat ground tracks indicate times when unusual high-frequency energy is detected in the CubeSat slant TEC measurements. We assume these times are associated with TIDs. This simple threshold-based detection maps the spatio-temporal evolution of the TIDs and it is consistent with the Lamb wave propagation. Note that not just the equatorial anomalies are detected but also the polar anomalies are detected after the atmospheric wave propagates through the poles; these detections in the polar regions require further study due to the complex geometries introduced at the poles and the radio ray paths and geomagnetic fields.

8. Prospect: Small Satellite Constellation for Geohazards

Low-lying and coastal regions in many countries are exposed to tsunami risk from the plate boundaries around the Pacific. A geohazard monitoring and advanced warning system based on a constellation of small satellites with GPS tracking is a low-cost and high technology readiness level concept that is an ideal companion complementary to the ground GNSS network by covering the ungauged area of the oceans and by delivering the upper ionosphere information. When both satellite and ground networks are combined, they can potentially bring substantial economic and environmental benefits to the international communities to save lives and protect infrastructure and resources.

An optimal small satellite constellation with preferably low inclination orbit will reduce re-visit time and enable rapid detection of TIDs excited by natural hazards. Incorporation of ground receivers such as the Guardian system (Martire et al., 2023) will be ideal to measure the whole spectrum of atmospheric disturbances. A (near) real time operation needs to be implemented for such a mission. Given the accuracy of International GNSS Service solutions for real-time and near-real-time GPS orbit and clock, as well as the Earth orientation parameter (EOP), the

use of ultra-rapid GNSS orbit and clock solutions and EOP for the near real-time POD should not hinder processing of ionospheric observations for TID monitoring. The uncertainty associated with the reference ionosphere model and its forcing parameters will be secondary since we are concerned only with perturbations in TEC. The critical aspect for real time operation is not on the technology at present but on logistics to secure GPS tracking data down-link as often as possible to multiple ground stations across multiple countries and to arrange immediate data transfer to processing units for near real-time POD and TEC computation and analysis for locating and characterizing geohazard sources.

Constellations of small satellites are rapidly expanding, including the CubeSat constellation of Spire Global and GeoOptics CICERO at present, and the 210 small satellite constellation from Skykraft in the near future (https://www.skykraft.com.au/news). These satellites are all tracked by GNSS and orbiting at diverse altitudes and inclinations. These space-borne networks of GNSS receivers will bring improved knowledge on processes in the upper atmosphere and help to monitor extreme events on the surface of the Earth. When co-ordinated internationally for real time operation, they can be used as an advanced hazard warning system by mitigating the impact of natural disasters and saving lives.

9. Conclusion

This study demonstrates that the upper atmosphere responds to impulsive forcing on the Earth's surface such as volcanic eruption. In this case, we study the Lamb wave from the HTHH eruption on 15 January 2022. We demonstrate that energy propagates from the ground to the ionosphere by examining traditional, yet unexplored, TEC data available from a number of nanosatellites orbiting at 500–600 km altitude (e.g., Spire Global's CubeSat constellation). We identify strong ionospheric perturbations in the upper atmosphere above ∼550 km altitude, as much as 10 TECU (measured as slant TEC between CubeSats and GNSS satellites), following the HTHH eruption around 04:30 UTC on 15 January 2022. The TID was recorded over India 12 hr after the major eruption and even further at the antipode near Algeria, North Africa almost 16 hr later. These suggest that the ionospheric disturbances traveled globally as a speed of ∼350 m/s. The significant disturbances at high altitudes remained as large as several TECU and clearly distinguished from the background variabilities. When processed with a total 15 CubeSat at the equatorial and polar orbits, we observe the spatio-temporal migration of the global TIDs; they generally follow the basic characteristics of the Lamb wave propagation.

In contrast to other TEC studies of the HTHH event based on the ground GNSS data, our analysis of space-borne TEC data provide unique information capturing only the high-altitude (>550 km) processes, that is complementary to stationary ground-borne TEC observations. The CubeSat TEC measurements represent the atmospheric disturbance at different locations by sampling wider region over a short period of time, rather than time series of TEC change at one place typically available from ground GPS receivers with a nearly constant transmitter-receiver geometry. Therefore, we suggest that this type of novel analysis will provide new knowledge on the dynamics of TIDs related to the interaction of solid Earth processes and the neutral atmosphere and ionosphere in conjunction with ground measurements (e.g., Dautermann et al., 2009; Mikesell et al., 2019). TID measurements at high altitudes (detectable from low Earth orbit satellites) are not yet exploited to study the upper atmosphere (>500 km), where the governing physics are less well known compared to lower altitudes. This provides us a new opportunity to improve our understanding, particularly of the upper part of the ionosphere, with the advent of small satellite technology.

Moreover, the space-borne receivers orbiting at the speed of 7–8 km/s can detect traveling acoustic and gravity waves related to geohazards such as tsunamis, faster, and more broadly than stationary ground-borne receivers. The real challenge is to discriminate the perturbations by different processes; for example, by geohazards or solar storms, and even for geohazard, by tsunami or atmospheric wave propagation. With improved knowledge on the coupled processes between solid Earth and upper atmosphere, the GPS measurements from a number of small satellites help develop new sensing modalities to utilize the whole atmosphere as a global sensor for the study of extreme natural hazards and lead to advanced warning systems.

Data Availability Statement

The Spire Global's GNSS/GPS tracking data sets (aka RINEX files) are publicly available via NASA's Commercial Smallsat Data Acquisition Program from the NASA program website https://csdap.earthdata.nasa.gov and also from the ESA's third party missions program https://earth.esa.int/eogateway/missions/Spire.

Acknowledgments
This work was funded by The University of Newcastle, Australian Research Council (DP160104095 and DP170100224), and in part by NASA's GRACE Follow-On science team project. We thank two anonymous reviewers for their careful reading and constructive comments which greatly improved the original manuscript. Of particular, the wave analysis like Figure 9 is indebted to one of the reviewers. LR is supported by French Agence Nationale de la Recherche (ANR) under reference ANR-19-CE04-0003 and Centre national d'études spatiales (CNES) for APR project UVTECGEOX.

References

Aa, E., Zhang, S., Erickson, P. J., Vierinen, J., Anthea, J., Goncharenko, L. P., et al. (2022). Significant equatorial plasma bubbles and global ionospheric disturbances after the 2022 Tonga volcano eruption. *Authorea Preprints*. https://doi.org/10.1029/2022SW003101

Afraimovich, E. L., Astafyeva, E. I., Demyanov, V. V., Edemskiy, I. K., Gavrilyuk, N. S., Ishin, A. B., et al. (2013). A review of GPS/GLONASS studies of the ionospheric response to natural and anthropogenic processes and phenomena. *Journal of Space Weather and Space Climate*, *3*, A27. https://doi.org/10.1051/swsc/2013049

Amores, A., Monserrat, S., Marcos, M., Argueso, D., Villalonga, J., Jorda, G., & Gomis, D. (2022). Numerical simulation of atmospheric Lamb waves generated by the 2022 Hunga-Tonga volcanic eruption. *Geophysical Research Letters*, *49*(6), e2022GL098240. https://doi.org/10.1029/2022gl098240

Astafyeva, E. (2019). Ionospheric detection of natural hazards. *Reviews of Geophysics*, *57*(4), 1265–1288. https://doi.org/10.1029/2019rg000668

Astafyeva, E., Maletckii, B., Mikesell, T. D., Munaibari, E., Ravanelli, M., Coisson, P., et al. (2022). The 15 January 2022 Hunga Tonga eruption history as inferred from ionospheric observations. *Geophysical Research Letters*, *49*(10), e2022GL098827. https://doi.org/10.1029/2022GL098827

Ben-Menahem, A. (1975). Source parameters of the Siberian explosion of June 30, 1908, from analysis and synthesis of seismic signals at four stations. *Physics of the Earth and Planetary Interiors*, *11*, 1–35. https://doi.org/10.1016/0031-9201(75)90072-2

Bilitza, D. (2018). IRI the international standard for the ionosphere. *Advances in Radio Science*, *16*, 1–11. https://doi.org/10.5194/ars-16-1-2018

Brissaud, Q., & Astafyeva, E. (2022). Near-real-time detection of co-seismic ionospheric disturbances using machine learning. *Geophysical Journal International*, *230*(3), 2117–2130. https://doi.org/10.1093/gji/ggac167

Calais, E., Bernard Minster, J., Hofton, M., & Hedlin, M. (1998). Ionospheric signature of surface mine blasts from Global Positioning System measurements. *Geophysical Journal International*, *132*(1), 191–202. https://doi.org/10.1046/j.1365-246x.1998.00438.x

Coïsson, P., Lognonné, P., Walwer, D., & Rolland, L. M. (2015). First tsunami gravity wave detection in ionospheric radio occultation data. *Earth and Space Science*, *2*(5), 125–133. https://doi.org/10.1002/2014EA000054

Dautermann, T., Calais, E., & Mattioli, G. S. (2009). Global Positioning System detection and energy estimation of the ionospheric wave caused by the 13 July 2003 explosion of the Soufrière Hills Volcano, Montserrat. *Journal of Geophysical Research*, *114*(B2), B02202. https://doi.org/10.1029/2008JB005722

Han, S.-C., McClusky, S., Li, T., Papanikolaou, T., Waters, C., & Pontin, D. (2021). A constellation of nanosatellites for geodesy, space weather and radio occultation experiment: Examples from Spire Global CubeSats. In *43rd COSPAR scientific assembly*.

Han, S.-C., McClusky, S., Mikesell, T. D., Tregoning, P., & Sauber, J. (2023). Looking to the sky for better tsunami warnings. *Eos*, *103*, 20–23. https://doi.org/10.1029/2022EO220519

Harkrider, D. G. (1964). Theoretical and observed acoustic-gravity waves from explosive sources in the atmosphere. *Journal of Geophysical Research*, *69*(24), 5295–5321. https://doi.org/10.1029/JZ069i024p05295

Harkrider, D. G., & Press, F. (1967). The Krakatoa air-sea waves: An example of pulse propagation in coupled systems. *Geophysical Journal of the Royal Astronomical Society*, *13*(1–3), 149–159. https://doi.org/10.1111/j.1365-246x.1967.tb02150.x

Heelis, R. A. (2004). Electrodynamics in the low and middle latitude ionosphere: A tutorial. *Journal of Atmospheric and Solar-Terrestrial Physics*, *66*(10), 825–838. https://doi.org/10.1016/j.jastp.2004.01.034

Heki, K. (2019). Ionospheric disturbances related to earthquakes. In C. Huang (Ed.), *Advances in ionospheric Research: Current understanding and challenges*. Wiley/AGU Book. Chapter 5-3.

Heki, K. (2022). Ionospheric signatures of repeated passages of atmospheric waves by the 2022 Jan. 15 Hunga Tonga-Hunga Ha'apai eruption detected by QZSS-TEC observations in Japan. *Earth Planets and Space*, *74*(1), 112. https://doi.org/10.1186/s40623-022-01674-7

Heki, K., & Ping, J. S. (2006). Directivity and apparent velocity of the coseismic ionospheric disturbances observed with a dense GPS array. *Earth and Planetary Science Letters*, *236*(3–4), 845–855. https://doi.org/10.1016/j.epsl.2005.06.010

Hickey, M. P., Schubert, G., & Walterscheid, R. L. (2009). Propagation of tsunami-driven gravity waves into the thermosphere and ionosphere. *Journal of Geophysical Research*, *114*(A8), A08304. https://doi.org/10.1029/2009JA014105

Hong, J., Kil, H., Lee, W. K., Kwak, Y.-S., Choi, B.-K., & Paxton, L. J. (2022). Detection of different properties of ionospheric perturbations in the vicinity of the Korean Peninsula after the Hunga-Tonga volcanic eruption on 15 January 2022. *Geophysical Research Letters*, *49*(14), e2022GL099163. https://doi.org/10.1029/2022GL099163

Jin, Y., Zhou, X., Moen, J. I., & Hairston, M. (2016). The auroral ionosphere TEC response to an interplanetary shock. *Geophysical Research Letters*, *43*(5), 1810–1818. https://doi.org/10.1002/2016GL067766

Kanamori, H., Mori, J., & Harkrider, D. G. (1994). Excitation of atmospheric oscillations by volcanic eruptions. *Journal of Geophysical Research*, *99*(B11), 21947–21961. https://doi.org/10.1029/94JB01475

Kherani, E., Lognonné, P., Hébert, H., Rolland, L., Astafyeva, E., Occhipinti, G., et al. (2012). Modelling of the total electronic content and magnetic field anomalies generated by the 2011 Tohoku-Oki tsunami and associated acoustic-gravity waves. *Geophysical Journal International*, *191*, 1049–1066. https://doi.org/10.1111/j.1365-246X.2012.05617.x

Komjathy, A., Galvan, D. A., Stephens, P., Butala, M. D., Akopian, V., Wilson, B., et al. (2012). Detecting ionospheric TEC perturbations caused by natural hazards using a global network of GPS receivers: The Tohoku case study. *Earth Planets and Space*, *64*(12), 1287–1294. https://doi.org/10.5047/eps.2012.08.003

Komjathy, A., Yang, Y. M., Meng, X., Verkhoglyadova, O., Mannucci, A. J., & Langley, R. B. (2016). Review and perspectives: Understanding natural-hazards-generated ionospheric perturbations using GPS measurements and coupled modeling. *Radio Science*, *51*(7), 951–961. https://doi.org/10.1002/2015rs005910

Kubota, T., Saito, T., & Nishida, K. (2022). Global fast-traveling tsunamis driven by atmospheric Lamb waves on the 2022 Tonga eruption. *Science*, *377*(6601), 91–94. https://doi.org/10.1126/science.abo4364

Lamb, H. (1911). On atmospheric oscillations. *Proceedings of the Royal Society of London. Series A, Containing Papers of a Mathematical and Physical Character*, *84*, 551–572. https://doi.org/10.1098/rspa.1911.0008

Lin, J., Rajesh, P. K., Lin, C. C. H., Chou, M., Liu, J., Yue, J., et al. (2022). Rapid conjugate appearance of the giant ionospheric Lamb wave signatures in the northern hemisphere after Hunga-Tonga volcano eruptions. *Geophysical Research Letters*, *49*(8), 1–6. https://doi.org/10.1029/2022GL098222

Martire, L., Krishnamoorthy, S., Vergados, P., Romans, L. J., Szilágyi, B., Meng, X., et al. (2023). The GUARDIAN system-a GNSS upper atmospheric real-time disaster information and alert network. *GPS Solutions*, *27*(1), 32. https://doi.org/10.1007/s10291-022-01365-6

Matoza, R., Fee, D., Assink, J. D., Iezzi, A. M., Green, D. N., Kim, K., et al. (2022). Atmospheric waves and global seismoacoustic observations of the January 2022 Hunga eruption, Tonga. *Science*, *377*(6601), 95–100. https://doi.org/10.1126/science.abo7063

Meng, X., Komjathy, A., Verkhoglyadova, O. P., Yang, Y.-M., Deng, Y., & Mannucci, A. J. (2015). A new physics-based modeling approach for tsunami-ionosphere coupling. *Geophysical Research Letters*, *42*(12), 4736–4744. https://doi.org/10.1002/2015GL064610

Meng, X., Vergados, P., Komjathy, A., & Verkhoglyadova, O. (2019). Upper atmospheric responses to surface disturbances: An observational perspective. *Radio Science*, *54*(11), 1076–1098. https://doi.org/10.1029/2019RS006858

Mikesell, T. D., Rolland, L. M., Lee, R. F., Zedek, F., Coïsson, P., & Dessa, J.-X. (2019). *IonoSeis*: A package to model coseismic ionospheric disturbances. *Atmosphere*, *10*(8), 443. https://doi.org/10.3390/atmos10080443

Omira, R., Ramalho, R. S., Kim, J., Gonzalez, P. J., Kadri, U., Miranda, J. M., et al. (2022). Global Tonga tsunami explained by a fast-moving atmospheric source. *Nature*, *609*(7928), 734–740. https://doi.org/10.1038/s41586-022-04926-4

Press, F., & Harkrider, D. G. (1962). Propagation of acoustic-gravity waves in the atmosphere. *Journal of Geophysical Research*, *67*(10), 3889–3908. https://doi.org/10.1029/jz067i010p03889

Rakoto, V., Lognonné, P., Rolland, L., & Coïsson, P. (2018). Tsunami wave height estimation from GPS-derived ionospheric data. *Journal of Geophysical Research: Space Physics*, *123*(5), 4329–4348. https://doi.org/10.1002/2017JA024654

Rolland, L. M., Vergnolle, M., Nocquet, J. M., Sladen, A., Dessa, J. X., Tavakoli, F., et al. (2013). Discriminating the tectonic and non-tectonic contributions in the ionospheric signature of the 2011, M_w 7.1 dip-slip Van earthquake, Eastern Turkey. *Geophysical Research Letters*, *40*(11), 2518–2522. https://doi.org/10.1002/grl.50544

Shults, K., Astafyeva, E., & Adourian, S. (2016). Ionospheric detection and localization of volcano eruptions on the example of the April 2015 Calbuco events. *Journal of Geophysical Research: Space Physics*, *121*(10), 10303–10315. https://doi.org/10.1002/2016JA023382

Themens, D. R., Watson, C., Žagar, N., Vasylkevych, S., Elvidge, S., McCaffrey, A., et al. (2022). Global propagation of ionospheric disturbances associated with the 2022 Tonga volcanic eruption. *Geophysical Research Letters*, *49*(7), e2022GL098158. https://doi.org/10.1029/2022GL098158

Wexler, H., & Hass, W. A. (1962). Global atmospheric pressure effects of the October 30, 1961, explosion. *Journal of Geophysical Research*, *67*(10), 3875–3887. https://doi.org/10.1029/jz067i010p03875

Zhang, S. R., Vierinen, J., & Goncharenko, L. P. (2022). Tonga volcanic eruption induced global propagation of ionopsheric disturbances via Lamb waves. *Frontiers in Astronomy and Space Science*, *23*. https://doi.org/10.3389/fspas.2022.871275

Zhao, Y., Deng, Y., Wang, J. S., Zhang, S. R., & Lin, C. Y. (2020). Tropical cyclone-induced gravity wave perturbations in the upper atmosphere: GITM-R simulations. *Journal of Geophysical Research: Space Physics*, *125*(7), e2019JA027675. https://doi.org/10.1029/2019JA027675